Process Mapping and In-Process Monitoring of Porosity in Laser Powder Bed Fusion using Layerwise Optical Imaging

Farhad Imani[2], Aniruddha Gaikwad[1], Mohammad Montazeri[1],

Prahalada Rao[1*], Hui Yang[2], and Edward Reutzel[3].

[1]Mechanical and Materials Engineering, University of Nebraska-Lincoln, Lincoln, NE
[2]Industrial and Manufacturing Engineering, Pennsylvania State University, State College, PA
[3]Applied Research Laboratory, Pennsylvania State University, State College, PA

Abstract

The goal of this work is to understand the effect of process conditions on part porosity in laser powder bed fusion (LPBF) Additive Manufacturing (AM) process, and subsequently, detect the onset of process conditions that lead to porosity from in-process sensor data. In pursuit of this goal, the objectives of this work are two-fold: (1) Quantify the count (number), size and location of pores as a function of three LPBF process parameters, namely, the hatch spacing (H), laser velocity (V), and laser power (P). (2) Monitor and identify process conditions that are liable to cause porosity through analysis of in-process layer-by-layer optical images of the build invoking multifractal and spectral graph theoretic features. This is important because porosity has a significant impact on the functional integrity of LPBF parts, such as fatigue life. Furthermore, linking process conditions to defects via sensor signatures is the first-step towards in-process quality assurance in LPBF. To achieve the first objective, titanium alloy (Ti-6Al-4V) test cylinders of 10 mm diameter × 25 mm height were built under differing H, V, and P settings on a commercial LPBF machine (EOS M280). The effect of these process parameters on count, size and location of pores was quantified based on X-ray computed tomography (XCT) images. To achieve the second objective, layerwise optical images of the powder bed were acquired as the parts were being built. Spectral graph theoretic and multifractal features were extracted from the layer-by-layer images for each test part. Subsequently, these features were linked to the process parameters using machine learning approaches. Through these image-based features, process conditions under which the parts were built was identified with the statistical fidelity over 80% (F-score).

Keywords: Laser Powder Bed Fusion, Porosity, In-process Monitoring, Image Analysis, Spectral Graph Theory, Multifractal Analysis.

---

[*] Corresponding Author – Prahalada Rao (email: rao@unl.edu)

1 Introduction

1.1 Background

Powder bed fusion (PBF) refers to a family of Additive Manufacturing (AM) processes in which thermal energy selectively fuses regions of a powder bed [1]. Figure 1 shows the schematic of the PBF process. A layer of powder material is spread across a build plate. Certain areas of this layer of powder are then selectively melted (fused) with an energy source, such as a laser or electron beam. The bed is lowered and another layer of powder is spread over it and melted [2]. This cycle continues until the part is built. The PBF process embodied in Figure 1 depicts a laser power source for melting the material, accordingly, the convention is to refer to the process as Laser Powder Bed Fusion (LPBF).

A galvanic mirror scans the laser across the powder bed. The laser is focused on the bed with a spot size on the order of 50 µm – 100 µm in diameter, the laser power is typically maintained in the range of 200 W to 400 W, the linear scan velocity of the laser is varied in the 200 mm/s to 2000 mm/s range, and the distance between each stripe of the laser, called the hatch spacing, is maintained in the range of 100 µm to 200 µm. The distance through which the bed is lowered is termed the layer height and is typically in the range of 30 to 50 µm. [2]. Close to 50 other parameters are involved in the melting and solidification process in LPBF [3].

Please insert Figure 1 here.

1.2 Motivation

The ability of LPBF to produce intricate geometry parts from hard-to-process materials, such as cobalt-chrome and nickel-based super alloys has been conclusively demonstrated for a variety of demanding applications ranging from biomedical to aerospace [4, 5]. Process repeatability and product quality, however, remain imposing barriers towards scaling LPBF to production environments [6]. Given the layer-by-layer nature of the process, a defect in a layer, if not averted, will be permanently sealed in by subsequent layers. These trapped defects adversely affect key functional properties of the part, such as its fatigue life and strength [7, 8].

A major gap in the current research lies in the lack of quantitative models to correlate the effect of process conditions on specific defects, such as porosity via the data acquired from in-situ sensors. Addressing this gap is the first-step towards in-process quality assurance in LPBF. Therefore, there is an urgent need to: (1) understand and quantify the effect of LPBF process conditions on defects, and (2) institute in-process sensing and monitoring to capture the onset of defects.

The following types of LPBF defects have attracted the most attention: porosity, surface finish, cracking, layer delamination, and geometric distortion. These defects are tracked to the following four root causes [9, 10]:

- Poor part design, such as inadequately supported features [11].
- Machine and environmental factors, such as poor calibration of the bed and optics.
- Inconsistencies in the input powder material, such as contamination and deviations in particle distributions.
- Improper process parameter settings, for example, inordinately high laser power causes vaporization of the material leading to keyhole porosity, while insufficient laser power prevents powder particles from fusing together leading to large acicular pores [12, 13]. This work specifically focuses on characterizing and detecting porosity in-situ due to the improper selection of process parameters.

1.3 Objectives

The goal of this work is to quantify the effect of process conditions on part porosity in the LPBF process, and subsequently, detect the onset of porosity due to deviation in process conditions based on in-process sensor data. An example of such a possible deviation is the occlusion of the optics due to vaporization of the material during melting and its eventual condensation on the focusing lens. The gradual coating of residue on the laser will lead to loss of laser focus, and hence reduce the power delivered to the substrate without the knowledge of the operator. In extreme instances, because the residue deposited on the lens absorbs a significant portion of the incident energy, damage to the lens and optical train can occur [14].

In pursuit of this goal, the objectives of this work are two-fold:

1. Quantify the effect of three LPBF process parameters, namely, laser power (P), hatch spacing (H), and velocity (V) on the size, count, and location of pores using X-ray computed tomography (XCT) scan data of the part.
2. Monitor and discriminate process deviations that are liable to cause porosity using in-process optical images of the powder bed invoking multifractal and spectral graph theoretic analysis.

The first objective is realized by simultaneously building nine titanium alloy cylinders on a commercial LPBF machine (EOS M280) at varying P, H, and V conditions, and quantifying their effect on the pore spatial distribution count, size and location are quantified using XCT images.

The second objective is achieved by acquiring layer-by-layer optical images of the parts while they are being built, and then extracting statistical, multifractal and spectral graph theoretic features from these images. These features are subsequently used in various classification approaches such as neural networks to ascertain their ability to isolate process conditions that are liable to produce parts with severe pores.

The rest of this paper is structured as follows. A brief review of the literature focusing on porosity and in-process sensing in LPBF is presented in Sec. 2; Sec. 3 describes the experimental conditions and layer-by-layer acquisition of part images; Sec. 4 explains the spectral graph theory and multifractal analysis of in-process image data for feature extraction and process modeling; and conclusions and avenues for future work are presented in Sec. 5.

2 Review of the Relevant Literature

The literature concerning the reasons and mechanisms of porosity formation and in-process sensing are summarized in Sec. 2.1 and Sec. 2.2, respectively.

2.1 Effect of LPBF process parameters on porosity

Of the various multi-scale defects in LPBF, porosity and its attendant causes have garnered the most attention [10, 15-17]. According to Rao *et al.*, voids or pores are empty spaces in a material and porosity is a measure of the volume occupied by these empty spaces over the total part volume [18]. Mechanical properties such as strength and fatigue performance LPBF-processed parts are severely affected by porosity; pores cause high-stress concentration, which in turn results in crack formation [19-22].

The formation of porosity is closely tied to and governed by the thermal phenomena at the meltpool-level [23]. Gong *et al.* have identified four distinctive regimes of melting contingent on the laser power (P) and velocity (V) process parameter settings. These regimes are demarcated as Zone I (fully dense); Zone II (over melting); Zone III (incomplete melting); and Overheating Zone (OH) [20, 24]. Visualizing a process map of laser power plotted on the ordinate axis, and the velocity on the abscissa, the region along the 45° slope falls under Zone I, also termed as the conduction mode. In this region, parts with least porosity-related defects were obtained. Zone II is to the left of Zone I, herein the laser power is higher for a given velocity compared to Zone I. This region is home to the so-called keyhole mode melting, where, as experimentally and theoretically elucidated by King *et al.* material vaporization occurs due to excessive energy input [25]. Zone III is to the right of Zone I, and is characterized by relatively higher velocity for a given power setting compared to Zone I. In this zone (Zone III), there is inadequate energy for the material to completely fuse.

While Gong *et al*. found that parts can be made in either of Zones I, II, and III, however, parts could not be built in the OH Zone, which is mapped to the left of Zone II, because the layers tend to deform to such a high degree during the build that the deposition of subsequent layers is impeded. Gong *et al.* report that in their experiments the recoater jams occurred in the OH zone due to contact with the part [20, 24]. Similar process mapping results for other AM processes, such as powder and wire-fed directed energy deposition, and electron beam powder bed fusion are reported by Beuth *et al.* [26-28]. Within the three melting zones, Zone I-III, the mechanism, and nature of pores formed are distinctive.

Lack of fusion porosity occurs in Zone III because the laser energy supplied is insufficient to fuse the adjacent tracks, and the current and previously deposited layers. Lack of fusion porosity results in the formation of large acicular pores of size in the range of 30 μm -100 μm [4]. From an experimental perspective for Titanium alloy Ti-6Al-4V, Gong *et al.* correlate areal energy density ($E_A = \frac{P}{H \times V}$ J/mm^2) with porosity and observed the onset of lack of fusion porosity typically occurs for $E_A < 1.1$ (approximately). Considering also the layer thickness T as a factor (maintained constant at 30 μm) the equivalent threshold for volumetric energy density $E_V = \frac{P}{H \times V \times T}$ is ≈ 36 J/mm^3.

Keyhole-collapse porosity in Zone II occurs due to vaporization of powder material [1-4]. King *et. al.* elucidate through theoretical simulations and experimental studies that when the energy supplied by the laser is inordinately high, the laser melts through several layers of the powder vaporizing material in its path. The vapor cavity eventually collapses thus forming pores deep within the meltpool [25]. The pores resulting from operating in the keyhole melting mode are uniform and circular in shape and are typically on the scale of 10-20 μm [12]. Gong *et al.*'s studies indicate that as the energy density in the processing of Ti-6Al-4V increases beyond a threshold value (typically $E_A > 2$, $E_V > 66$) the process enters the keyhole melting mode [20, 24].

To avoid oxidation of the powder, the LPBF process is carried out in a chamber filled with inert gas (usually argon or nitrogen) depending upon the material to be processed. The argon or nitrogen gas may get trapped in the powder and lead to the formation of gas pores [29]. Additionally, gas pores are also formed when bubbles are trapped in the meltpool during the solidification process [18]. Gong *et al.* also explain the formation of voids and pits due to the ejection of powder material as spatter on account of the thermal energy [20, 24]. The ejected particles may settle within the boundary of the part, and on cooling may adhere to the surface of the powder bed. Further, as the next layer is being deposited, the adhered particles may subsequently be removed by the recoater leaving a pit or void in its place. Lastly, lower melting impurities and constituents may vaporize given a sufficiently high energy density (and not due to keyhole collapse) leaving voids in the part [30]. Such types of pores are not restricted to one type melting zone and are stochastic in nature.

From the extensive experimental work of Gong *et al.* it is surmised that for Ti-6Al-4V material, the conduction melting mode typically occurs in the range of $1.1 < E_A < 2$ J/mm^2; or equivalently $36 < E_V < 66$ J/mm^3. Aboulkhair *et al.* [12, 31] and Stucker *et al.* [32-34] report extensive process optimization studies related to porosity in LPBF with conclusions in line with findings by Beuth *et al* [26-28]. While most of the existing process maps relate the effect of areal or volumetric energy density to porosity with the aid of X-ray computed tomography (XCT), a conspicuous gap remains in relating pore size, density and location simultaneously with E_A. This work addresses the foregoing gap through Objective 1.

In closing this section, we note that the process zones and concomitant types of porosity reported in the literature are contingent on the presumptions of stable process operation and that the part geometry and its location on the build plate have negligible effect.

2.2 Sensing and Monitoring in LPBF

Comprehensive review articles for in-process sensing are available in Ref. [9, 35-38]. Significant research in process sensing and control for metal AM processes is being done in academe and national laboratories [39-44]. Nassar and Reutzel, *et al.* experimented with imaging of the LPBF powder bed under various illumination conditions [41, 44, 45]. The resulting layer data was analyzed, and defects, such as voids caused by improper raking of the powder across the bed were identified. Lane *et al.* at NIST integrated an LPBF machine (EOS M270) with thermal and high-speed cameras, and a photodetector [39]. NIST and Edison Welding Institute (EWI) are currently building a customized LPBF testbed instrumented with multiple sensors [43, 46]. A large body of work in sensing and monitoring in LPBF is reported by the Kruth group [47-49] and Witt group [50-53] in Europe. Recent breakthroughs with in-situ X-ray imaging of the LPBF process has been reported by scientists at Lawrence Livermore National Laboratories [54].

To detect evolving process anomalies researchers have sought to incorporate sensing techniques such as vibration, CCD video imaging, infrared and ultraviolet imaging, pyrometers, photodiodes, ultrasonic wave generators in AM machines [50, 55-61]. An early example was presented by Melwin *et al.* [62], who used a video-micrography apparatus bearing band pass and polarizing filters for observing the meltpool in polymer LPBF.

In a series of related works, Craeghs *et al.* [47-49] describe optical-based approaches for monitoring build quality in PBF by imaging the thermal behavior at the meltpool. Craeghs *et al.* were able to detect process defects, such as deformation and overheating using their optical system [48]. Bartkowiak [63] describes a PBF apparatus integrated with a spectrometer for *in situ* measurements of the layer melt characteristics, such as emissivity. Other researchers, e.g., Chivel *et al.* [64], and Jacobsmuhlen *et al.* [50] have also developed optical imaging systems for process monitoring in AM [64]. In a recent work, Rieder *et al.* [58] used an ultrasonic sensing system for tracking build status in PBF. A broadband ultrasonic sensor mounted on the underside of the build plate is used to detect voids, akin to acoustic microscopy.

Craeghs *et al.* [48, 65, 66] report that the amplitude of the photodiode signal is correlated with the melt-pool area and the melt-pool temperature. They subsequently use this information to identify process failures, such as detection of deformation due to thermal stresses and overheating at overhang structures, in each build layer. Further, they developed a feedback control sensor based on optical images. Chivel and Smurov [64] use two different wavelengths and selected temperature profiles to extract information of the bed temperature distribution, and the size of the meltpool for process monitoring.

Regarding the fidelity of the different sensing approaches for detecting defects specific to PBF AM processes, the viability of thermal imaging and optical spectroscopy-based techniques has been demonstrated in the literature. Recent work done by researchers at NIST aims to comprehensively capture the effect of meltpool shape and thermal gradients to defects. From the meltpool monitoring vista, a fast response thermal camera with a high framerate (> 1000 frames/second) and resolution in the micrometer range is typically used to circumvent blurring effects [67]. In recent work by EWI researchers the meltpool-level thermal camera is coupled with another thermal camera that monitors the heat flux over the entire bed to detect large macro-scale defects, such as warping [46]. However, such high-fidelity thermal cameras are exceeding expensive, and moreover, they are appropriate for capturing thermal trends rather than the exact temperature of the target because the emissivity of the meltpool remains to be established. Dual color pyrometers can be used to circumvent the lack of emissivity information.

A far less expensive alternative to thermal imaging for detection of micrometer-level defects is through the use of photodetectors and spectrometers. Nassar *et al.* in a series of articles demonstrate the use of such optical emission spectroscopy-based sensing [42, 68, 69]. The key idea is to measure the intensity (amplitude) of the line-to-continuum ratio emission spectra of the material being processed and relate the readings to part defects. For this purpose, two photodetectors are coupled through a 50:50 beam splitter, and focused upon the entire bed area. Each of the photodetectors is fitted with an optical bandpass filter that captures light corresponding to the emission spectra of a particular element in the alloy being processed. For instance, for detecting anomalies in LPBF of Inconel 718, Nassar *et al.* used a 520 nm ± 5 nm and 530 nm ± 5 nm optical bandpass filters corresponding to the continuum and line spectra, respectively, of Cr I emissions [68].

Instead of using two photodetectors to capture formation of porosity, Montazeri *et al.* in two articles published in this journal, have used a single photodetector to capture the onset of material contamination, and also to distinguish the process signatures emanating for different feature geometries, such as overhang-related features [30, 70]. While photodetectors and spectrometers present a cost advantage over thermal imaging, and are capable of sampling rates nearing 1 MHz, their main drawback is that the output is in terms of a time series or frequency spectrum which have far limited information compared to thermal imaging.

In this context, the use of optical imaging for detection of conditions liable to produce porosity is a novel contribution of this work. Optical imaging cameras are significantly less expensive than their thermal and high-speed counterparts. However, the challenge of capturing pores directly from the layerwise optical images, as opposed, to the anomalous process conditions has not yet been attempted. In closure, we note that Abdelrahman *et al.* [45] have used optical imaging data to capture the large-scale (> 100 μm) defects which were deliberately introduced during the build.

The main drawback in most of these studies is that they do not connect practical process conditions to defects, but rather focus on artificially inducing flaws by way of catastrophic process anomalies. Furthermore, the analytical techniques rely on classical time-series signal processing techniques, which may not be effective in capturing subtle defects. Recent progress to overcome this limitation is reported by the Clare group at Nottingham University who have used spatially resolved acoustic spectroscopy (SRAS) to detect porosity ex-situ in LPBF, wherein the amplitude of a surface acoustic wave generated by laser is correlated with the location and severity of porosity at different laser power settings [71, 72]. The current work addresses this extant gap through Objective 2.

3 Experimental Setup and Data Acquisition

Experiments were conducted on an EOS M280 LPBF machine. The input material was a Titanium alloy, ASTM B348 Grade 23 Ti-6Al-4V powder material whose particle size ranges from 14 μm to 45 μm. The parts analyzed in this study are cylinders which were printed by varying the hatch spacing (H), scan velocity (V) and laser power (P). The cylinders are 25 mm in length and 10 mm in diameter. shows the seven process parameter settings which were used to print these cylinders. The nominal settings are labeled as H0 = 0.12 mm, V0 = 1250 mm/s, and P0 = 340 W. The layer height is maintained is constant at T = 60 μm. Hatch spacing and laser print velocity are increased by 25% and 50%, and laser powder has been decreased by 25% and 50% from their nominal settings. The three process settings are aggregated in terms of the areal energy density applied for melting called the Andrew number: $E_A = \frac{P}{H \times V}$ J/mm^2 or the volumetric energy density $E_V = \frac{P}{H \times V \times T}$. Comparing the E_V values reported in Table 1 with the experimental results of Gong *et al.* [20, 24], we note that barring the nominal settings, which is set in the conduction regime (Zone I), all other experimental treatment combinations fall within the lack of fusion (Zone III) regime where acicular pores are expected ($E_V < 36$).

A digital single-lens reflex camera (DSLR, Nikon D800E) along with multiple flash-lamps placed inside the build chamber is used to capture the layer-by-layer powder bed images. Images are captured at two instances in every layer, namely, post laser scan and post re-coat. The camera shutter is controlled by a proximity sensor that registers the location of the re-coater blade. Five images of the powder bed images are captured under bright-field and dark-field flash settings. The layout of the camera and flash-lamp location are shown in Figure 2, and the representative images under the five light schemes are shown in Figure 3. In this work, images from the bright-field light scheme in Figure 3(a) are analyzed. Details of the experimental setup are available in Ref. [45].

Please insert Table 1 here.

Please insert Figure 2 here.

Please insert Figure 3 here.

4 Methodology and Results

As shown in Figure 4, the LPBF process data is analyzed in two phases, namely, (1) offline analysis of X-ray computed tomography (XCT) data in Sec. 4.1; and (2) analysis of in-situ images of the powder bed in Sec. 4.2.

Please insert Figure 4 here.

4.1 Phase 1: Offline analysis of porosity.

This section aims to analyze the effect of hatch spacing (H), laser velocity (V), and laser power (P) on the count, size, and location of pores. Representative XCT images of parts under different P, H and V conditions are shown in Figure 5. A visual inspection of the XCT scans shows that the size and number (count) of the pore is inversely proportional to the areal energy density (EA).

As the areal energy density (Andrew's number, E_A) is reduced, we observed that the size and number of the pores become larger. However, we caution that, although, the critical process parameters, such as laser power (P, Watt), hatch spacing (H, mm), scan velocity (V, mm/sec), and layer height (mm) can be optimized for certain part geometries, and aggregated in terms of the global volumetric energy density (E_A) pores can still occur. This is because, E_A does not account for the thermal aspects in the part (heat flux), which is contingent on the part geometry, orientation, and its location on the build plate. For instance, parts in the far edge of the build platen (near the end of the recoater action) may suffer from insufficient powder feed (powder shorting), likewise, the laser spot size is liable to change as the laser tends to defocus on the outer edge of the build platen leading to lack-of-fusion related porosity.

Furthermore, there is the possibility of a complex, nonlinear interaction between P, V, and H which remains as yet undiscovered and therefore not captured in the relationship representing the areal energy density (EA). For instance, in the equation for EA, all terms are assumed to be equal in weight, i.e., the exponent P, V, and H is unity (=1) and therefore the relationship between EA and the process parameters is implicitly assumed to be a simple linear relationship. The following inference is made based on Figure 5. For instance, while the severity of pores is influenced by all three process parameters. However, laser power (P) seems to have an inordinately high effect. This observation is further quantified by extracting count, size and location attributes by analyzing the XCT scan images through the steps shown in Figure 6.

- Figure 6 (a) - XCT scans for 30 randomly chosen cross-sectional areas are analyzed.
- Figure 6 (b) and (c) - The XCT scan images are binarized based on a heuristically determined threshold. Some information is inevitably compromised during the binarization process. A complement of the binary image is taken to return a black background, which makes computation easier as the image matrix becomes sparse.
- Figure 6 (d) - To reduce noise induced due to binarization the nearest neighborhood approach is used [73]. We note that while it is customary to refer to voxels in the context of XCT, because the images are converted to binary images (binarized), we revert to using the term pixel. In this procedure, a binarized XCT pixel is labeled as a defect only if it is connected to the 8-nearest pixels. In other words, if the 8 nearest neighboring pixels of a particular pixel are also bright (i.e., 1), then the pixel is deemed to represent part of a defect.

Please insert Figure 5 here.

Please insert Figure 6 here.

Next, the pore count, size and location are extracted as follows:

- Pore count – The number of 8-connected binarized XCT pixel over a layer translates to the pore count.
- Size of pores – The size of a pore is grouped into one of 5 classes contingent on its radius. Each pore is considered as an annular structure on the noise reduced image, and then, the number of pixels within each annulus is calculated. Depending on the number of pixels in the annulus, the pores are classified into various radii, namely 1-5 pixel radii. A radius of one-pixel unit equates to a pore radius of 16 μm on the part.
- Pore Location – The pore location is determined by segmenting the XCT scan image into 5 concentric areas as shown in Figure 7. The number of pores in each 1-mm thick segment of the XCT scan image is then counted. This establishes the distance of the pores from the center of the cylinder.

Please insert Figure 7 here.

(a) Effect of process parameters on count and size of pores

Analysis of the XCT scan images shows that decrease in the areal energy density (EA) leads to an increase in the count (number of pores) and size of pores. This effect of laser power (P), hatch spacing (H), and laser print velocity (V) on pore count and size are exemplified in Figure 8 from which the following inferences are drawn. In Figure 8, the x-axis is the pore size, and the y-axis is the mean count (or number) of the pore observed on 30 randomly selected slices of the XCT scan. These results are also detailed in Table 2, which reports the mean number of pores, rounded to the nearest integer, along with the standard deviation for 30 randomly chosen layers.

- Referring to Figure 8 (a), the pore distribution in terms of count vs. pore size is plotted for different levels of laser power (P). The decrease in laser power by 50% (170 W) leads to almost a 100-fold increase in the number of pores. Further, parts produced under P -50% (170 W) have pores ranging from 1 pixel to 4 pixels in size, i.e., 28 μm to 112 μm, whereas parts produced under nominal power (P0= 340 W) and P -25% (270 W) have pores of radius 2 pixels (~ 32 μm) at most.
- Referring to Figure 8 (b), increasing the hatch spacing (H) leads to an increase in both the count and size of pores. The magnitude of the effect of laser hatch spacing is significantly smaller than that of laser power. In case of varying hatch spacing (Figure 8 (b)), the highest number of pores are seen in the cylinder which is printed with H +50 %, i.e., 0.18 mm hatch spacing. From Figure 8 (b), for all the three levels of hatch spacing, the largest pore radius observed is 2 pixels.
- Referring to Figure 8 (c), akin to hatch spacing, increase in laser print velocity (V) leads to increase in count and size of pores. The largest pore size of radius 3 pixels (~48 μm) was recorded in the cylinder printed with V +50 % (1875 mm/s). The effect of velocity on porosity is least consequential of the three factors studied in this work.

Please insert Figure 8 here.

Please insert Table 2 here.

(b) Effect of process parameters on the location of pores

The location of pores in the test cylinders is determined by segmenting the XCT scan image of a cylinder into 5 concentric parts as described previously in the context of Figure 7. This establishes the distance of the pores from the center of the cylinder. The mean and standard deviation of pores in each segment of the part for 30 randomly chosen layers are reported in **Error! Reference source not found.** and depicted in Figure 9, from which the following inferences are drawn:

- Referring to Figure 9 (a), it is evident that as the laser power decreases, more number of pores are recorded in the L_2 (4 mm – 8 mm) to L_4 (8 mm – 12 mm) segment, of the cylinder. Figure 9 (a) further reveals that the cylinder printed with nominal laser power (340 W) has most number of pores in the first two annular segments of length L_1 (0 mm – 4 mm) and L_2 (4 mm – 8 mm), which indicates that the pores are located close to the center. This trend is also observed in the cylinder printed with P -25 % laser power (270 W). In contrast, the cylinder printed with -50 % laser power has most number of pores in the third segment 8-12 mm.
- Referring to Figure 9 (b) and (c), in cylinders printed with varying hatch spacing (H) and laser print velocity (V), respectively it is observed that parts produced at +50% hatch spacing (0.18 mm) and laser print velocity (1875 mm/s) have the highest number of pores at the radial distance with L_3 (8-12 mm). Pores in the cylinders printed with +25% and nominal hatch spacing and laser print velocity are mainly located in the first two segments 0 mm - 1 mm and 1 mm - 2 mm.

The sharp drop in porosity in L5 is likely due to the reason that the external boundary of the part is scanned with increased EA after the rest of the part (post-contour melting). The added heat at the periphery mitigates porosity in L5. Further, the concentration of heat in the core of the part may explain the reduced porosity towards the center (L1). Lastly, the effect of thresholding to convert may lead to a loss of information, this last reason can be largely discounted in the light of Figure 6 (a and d), wherein pores in the boundaries are captured appreciably.

Please insert Figure 9 here.

Please insert Table 3 here.

4.2 Phase 2: Analysis of online data of laser powder bed fusion process (LPBF).

This section aims to link the process conditions to the layer-by-layer images of the parts as they are melted. This will allow detection of process drifts in their early stages. For this purpose, two methods are proposed, the first based on spectral graph theory, and the second using multifractal and lacunarity analysis.

(a) Application of spectral graph theory for part image analysis

Spectral graph theoretic Laplacian eigenvalues extracted from online images are used to identify the process conditions under which a part is produced. The approach has the following two steps.

Step 1: Representing the image of each part as a graph.

A layer-wise image obtained from the DSLR camera for a laser sintered cylinder layer with M × N pixels can be represented by a matrix $\boldsymbol{X}^{M \times N}$. As shown in Figure 10, each row of the matrix X

is considered as a row vector and it represents a node or vertex (V) of an undirected graph which is denoted as $G \equiv (V, E)$, where E is the edges in the graph [74]. The M row vectors of the matrix X are represented as $\boldsymbol{a}_K, K = \{1,2, \ldots \mathrm{M}\}$.

Please insert Figure 10 here.

Further, a pairwise comparison is performed between each of the row vectors through a kernel function Ω [75]. A pairwise comparison along the columns has been shown to lead to similar results as long as the image is homogeneous [76].

$$w_{pq} = \Omega\left(\overrightarrow{a_p}, \overrightarrow{a_q}\right) \forall\, p, q \in K \tag{1}$$

The kernel function Ω used in this study to compute the pairwise comparison is the radial basis kernel function (Eqn. (2) and (3)) .

$$w_{pq} = e^{-\left[\frac{\boldsymbol{E}}{\sigma_X}\right]^2} \tag{2}$$

$$\boldsymbol{E} = \left[\left\|\overrightarrow{\boldsymbol{a}_p} - \overrightarrow{\boldsymbol{a}_q}\right\|^2\right] \tag{3}$$

where, σ_X is the overall standard deviation of E. Next, a binary similarity matrix $\boldsymbol{S} = \left[w_{pq}\right]$ is created with help of a threshold function. This threshold function θ when applied to w_{pq} converts it into binary form[77].

$$\Theta\left(w_{pq}\right) = \mathrm{w}_{pq} = (0,1) \tag{4}$$

This threshold function facilitates in determining whether there is a connection between two nodes [77]. w_{pq}= 1 if there is a connection and otherwise it is zero.

$$\Theta\left(w_{pq}\right) = \mathrm{w}_{pq} = \begin{cases} 1, w_{pq} & \leq r \\ 0, w_{pq} & > r \end{cases} \tag{5}$$

Here r is given by,

$$r = \frac{\sum_{p=1}^{p=\mathrm{M}} \sum_{q=1}^{q=\mathrm{M}} \mathrm{w}_{pq}}{\mathrm{M}^2} \tag{6}$$

Step 2: Extracting features from the graph.

Once a graph is formulated from the image, topological features are extracted from the graph. These features are useful in classification of parts which are made with different process parameters. The first step towards feature extraction is computing the degree d_p of a node p, i.e., the number of edges that pass through the node p. The degree of node p is computed by summing each row in the similarity matrix $\boldsymbol{S}$. From the degree of node d_p, a diagonal degree matrix $\boldsymbol{\mathcal{D}}$ is formed as follows,

$$\boldsymbol{\mathcal{D}} \overset{\text{def}}{=} \operatorname{diag}(d_1, \cdots, d_M) \tag{7}$$

Now, with the help of the degree $\boldsymbol{\mathcal{D}}$ matrix and the similarity matrix $\boldsymbol{S}$, the normalized Laplacian $\boldsymbol{\mathcal{L}}$ of the graph is defined as follows,

$$\boldsymbol{\mathcal{L}} \overset{\text{def}}{=} \boldsymbol{\mathcal{D}}^{-\frac{1}{2}} \times (\boldsymbol{\mathcal{D}} - \boldsymbol{S}) \times \boldsymbol{\mathcal{D}}^{-\frac{1}{2}} \tag{8}$$

where, $\boldsymbol{\mathcal{D}}^{-\frac{1}{2}} = \operatorname{diag}\left(1/\sqrt{d_1}, \cdots, 1/\sqrt{d_M} \right)$.

Finally, the Eigen spectra of the Laplacian is computed as follows [78].

$$\boldsymbol{\mathcal{L}v} = \lambda^* \boldsymbol{v} \tag{9}$$

The eigenvalues (λ) of the Laplacian are used in the classification of LPBF parts per their processing conditions. In this work, the first five smallest non-zero eigenvalues are used. Also, the Kirchhoff index for each graph is computed as follows, where λ_i are the non-zero eigen values of the Laplacian.

$$K_f = 2 \times \varepsilon \times \sum_{i=2}^{\mathrm{M}} \lambda_i^{-1} \tag{10}$$

where $\varepsilon = \frac{\sum_{i=1}^{i=M}\sum_{j=1}^{j=M} s_{ij}}{2}$.

The non-irradiated part of the part image i.e. the un-sintered powder, is fairly homogenous, so when it the image undergoes a row-wise comparison, the distance kernel function becomes zero [79]. The nodes which are far apart from each other are connected on the graph.

(b) Multifractal and lacunarity analysis of part images

The fractal dimension has been extensively used to characterize the texture and patterns of manufactured surfaces [17, 80-83]. This work goes beyond the traditional methods that extract a single fractal dimension from the surface image, but rather assume the irregularity and non-homogeneity of image data are due to the presence of several fractal dimensions [83]. As such, we extract a spectrum of multifractal features to characterize the layer-by-layer images obtained in LPBF. A fractal is defined as a shape that embodies geometric similarity across multiple scales [84-86]. Assuming that a fractal object occupies a limited area in the Euclidean space, then the object can be covered by N measure elements with size ε as follows,

$$N(\varepsilon) = \varepsilon^{-D} \tag{11}$$

where D is the fractal dimension. The box-counting method is widely used to estimate the fractal dimension of an irregular object. This method covers a fractal set with measure elements (e.g., box) at different sizes and observes how the number of boxes varies with its size [87]. This procedure is repeated using different boxes of size l. Once the l becomes sufficiently small, N(l) being the number of boxes that are needed to cover a fractal object with the size l, then the box-counting dimension D_0 is defined as,

$$D_0 = \lim_{l \to 0} \frac{\ln N(l)}{\ln\left(\frac{1}{l}\right)} \tag{12}$$

Please insert Figure 11 here.

For example, Figure 11 shows three types of fractal objects called multifractal trees that are constructed with the iterated function systems (IFS) method. These fractal trees are labeled T1, T2, and T3. The estimates of fractal dimension (D_0) using the box-counting method in Figure 11 are $D_0 = 2.0449$ for all three fractal trees. However, three trees show high levels of self-similarity, irrgularity and heterogeneity due to the presence of a spectrum of fractal dimensions. This demonstrates that the traditional box-counting fractal dimension is limited in the ability to fully characterize the patterns of multifractal objects [88]. Multifractal analysis provides a means to overcome this limitation of traditional fractal dimensions. The procedure to estimate the multifractal spectrum from image data is as follows,

Step 1: Estimating the local densities function ($P_i(L)$).

$$P_i(L) = \frac{N_i(l)}{N_T} \tag{13}$$

where $N_i(l)$ is the number of mass or pixels in the ith box of size l, N_T is the total mass of a set and $P_i(l)$ is the probability in the ith box.

Step 2: Calculating singularity strength exponent (l^{α_i}).

$$P_i(l) \sim l^{\alpha_i} \tag{14}$$

where α_i reflects the local behavior of Pi (l) in the ith box with size l and it can be derived as

$$\alpha_i = \lim_{l \to 0} \frac{\ln P_i(l)}{\ln l} \tag{15}$$

Step 3: Estimating multifractal spectrum ($f(\alpha)$).

The multifractal spectrum $f(\alpha)$ is the fractal dimension of the set of locations that have same values for singularity strength exponents α_i. Given the number of boxes $N(\alpha)$ where the probability $P_i(l)$ has exponent values between α and $\alpha + d\alpha$ the multifractal spectrum $f(\alpha)$ can be calculated as follows,

$$f(\alpha) = \lim_{l \to 0} \frac{\ln N(\alpha)}{\ln(1/l)} \tag{16}$$

Step 4: Characterizing multifractal measures (D_q).

Multifractal measures are characterized by the scaling of the qth moments of $P_i(l)$ distributions as,

$$\sum_{i=1}^{N(l)} P_i^q(l) = l^{\tau(q)} \tag{17}$$

where $\tau(q)$ is called the mass exponent of qth order moment. Then, the generalized fractal dimensions D_q can be written as,

$$D_q = \frac{\tau(q)}{q-1} \tag{18}$$

Then, the Legendre transformation is used to derive the multifractal spectrum as,

$$f\big(\alpha(q)\big) = q\alpha(q) - \tau(q) \tag{19}$$

$$\alpha(q) = \frac{d\tau(q)}{dq} \tag{20}$$

However, Legendre transformations are computationally demanding in the calculation of $f(\alpha)$. Also, this approach requires smoothing the D_q curvthe e which causes errors in the estimated $f(\alpha)$ [89]. To overcome this limitation and bypass intermediate smoothing steps in estimating $f(\alpha)$, a family of normalized measures $\mu_i(q,l)$ as qth moments of mass probability Pi(l) are introduced in Eqn. (21). A constant l range is also used to avoid multifractal properties over a small interval of scales.

$$\mu_i(q,l) = \frac{P_i^q(l)}{\sum_{i=1}^{N(l)} P_i^q(l)} \tag{21}$$

As such, the multifractal spectrum $f(\alpha)$ and the average singularity strength exponent $\alpha(q)$ can be written as,

$$f\big(\alpha(q)\big) = \lim_{l\to 0} \frac{\sum_{i=1}^{N(l)} \mu_i(q,l)\ln[\mu_i(q,l)]}{\ln l} \tag{22}$$

$$\alpha(q) = \lim_{l\to 0} \frac{\sum_{i=1}^{N(l)} \mu_i(q,l)\ln\left[P_i^q(l)\right]}{\ln l} \tag{23}$$

Figure 12 shows the multifractal spectra for three IFS trees in Figure 11. It is evident that multifractal features effectively distinguish the differences in the three IFS trees that were not captured using the traditional fractal dimension. Note that the tail of the third IFS tree T3 is longer than other two IFS trees. Because T3 has more pixels with lower values (value towards 0 or black pixels) in comparison to the other two trees and the $f\big(\alpha(q)\big)$ spectrum intensifies the effect of pixels with lower values.

Please insert Figure 12 here.

Furthermore, lacunarity complements multifractal analysis by characterizing the manner or distribution in which the fractal objects fill the space [90, 91]. Lacunarity and multifractal analysis jointly describe the irregularity and non-homogeneity in fractal objects as well as how they fill the space that cannot be otherwise achieved by traditional box-counting dimension or statistical features. To obtain the lacunarity measure, a unit box of size l is placed over the object and the number of set points s (black pixels) in the image is counted – this is called the box mass. Next, the box is translated one space along the set, and the box mass is again determined. This process is repeated over the entire set, creating a frequency distribution of the box masses represented as N(s,l). This frequency distribution is converted into a probability distribution Q(s,l) by dividing by the total number of boxes N(l) of a given size l [92].

$$Q(s,l) = \frac{N(s,l)}{N(l)} \tag{24}$$

The first and second moments of this distribution can be written respectively as:

$$Z_1 = \sum sQ(s,l) \tag{25}$$

$$Z_2 = \sum s^2Q(s,l) \tag{26}$$

The lacunarity method with box size *l* can be computed as:

$$\Lambda(l) = \frac{Z_2}{(Z_1)^2} \tag{27}$$

In Eqn. (24), *Λ(l)* represents the lacunarity for the box size *l*. This procedure is repeated for different box sizes, and a log-log plot of the lacunarity versus the size of the box is traced. Figure 13 shows T3 has higher lacunarity values in comparison to the two other trees. The distribution of gap sizes is termed as lacunarity.

Figure 14 shows the singularity strength exponent *α(q)* and multifractal spectrum *f(α(q))* estimated from 3132 layerwise images in the LPBF process. There are 1044 images in E_A=2.27; 696 in E_A=1.81; 348 in E_A=1.70; 696 in E_A=1.51; and 348 in E_A=1.13. Note that multifractal spectra of these images show significant variations with respect to the different Andrew's numbers.

Please insert Figure 13 here.

Please insert Figure 14 here.

4.3 Application of Multifractal and Spectral Graph Theory to Online Images

Further, the parts built under the different E_A conditions described in Table 1 were classified using different machine learning approaches with various types of input features. A 70%-15%-15% split for training, testing, and validation data were imposed. The classification fidelity is reported in terms of the F-score, which is an aggregate of the Type I and Type II statistical errors. The results are summarized in Table 4.

Please insert Table 4 here.

Three types of input features are used: (1) statistical image features, namely, intensity (mean) of an image, and local standard deviation of an image in 3 × 3 neighborhood, (2) spectral graph theoretic features, namely, the first five non-zero Eigenvalues and the Kirchhoff index, and (3) the multifractal and lacunarity features. It is observed that irrespective of the classification approaches used, the spectral graph and multifractal and lacunarity features outperform the conventional statistical features. Furthermore, combining the spectral graph and multifractal features results in F-score around 80%. The results reported in Table 4 show that the spectral graph theoretic and multifractal features discriminate the part quality with higher fidelity than traditional statistical analysis. This is valuable from the in-process quality monitoring viewpoint. In a practical scenario, images of the parts can be used to conclude whether the process within an optimal window.

5 Conclusions and Future Work

This paper presents the modeling and analysis of in-process layerwise images in LPBF to investigate the effect of LPBF process conditions on the severity, size, and location of porosity, and further connects the process conditions to sensor signatures. This is an indirect way to monitor the LPBF process. The specific outcomes of the work are as follows:

1. Three process parameters, namely, laser power (P), hatch spacing (H), and scan velocity (V) were varied during the LPBF of Ti-6Al-4V powder material. The effect of varying these parameters on porosity was characterized offline using X-ray computed tomography (XCT). Based on analysis of the XCT images the following inference is tendered. Decreasing the laser power by 50% from 340 W to 170 W leads to almost a three-fold increase in the average number of pores, compared to an equivalent percentage increase in hatch spacing, and ten-fold increase compared to scan velocity. Hence, the control of laser power is most consequential for avoiding porosity.
2. Online visible spectrum images of the part were acquired as they are built using a still camera. These images were analyzed using multifractal and graph theoretic approaches. The features extracted by applying these approaches were subsequently used within various machine learning techniques. The aim was to distinguish the process conditions under which the parts were built given an image of the part. It is observed that combining multifractal and graph theoretic analysis leads to as much as 30% increase in the accuracy of discriminating process conditions compared to using traditional statistical measurements. Using this approach, the process conditions can be isolated with F-score approaching 80%. From a practical perspective, although the P, H, and V settings are predetermined for each material in terms of the Andrew number (E_A), the laser power, particularly, is liable to drift due to occlusion of

the focusing optics; the vaporized material tends to condense on the lens especially during long builds.

One limitation of this work is that it does not relate the sensor signatures directly to the defects, but rather isolates the process condition that leads to porosity. This is mainly due to the fact that the resolution of the camera is not sufficient to identify pores, which are in the 16 µm – 65 µm, from the images directly. To overcome this drawback, data from multiple sensors will be combined (e.g., thermography and meltpool monitoring) to not only capture multiple types of defects simultaneously but also improve upon the detection fidelity. Furthermore, in the future work, the authors will endeavor to understand the effect of process parameters on other type of defects, such as distortion and geometric inaccuracy.

Acknowledgements

The authors acknowledge the help provided by Mr. Cheng-Bang Chen (Penn State), Mr. Ben Bevans (UNL), and Ms. Emily Curtis (UNL) in the analysis of X-ray computed tomography images. This work is supported in part by the National Science Foundation (NSF) Center for e-Design (Lockheed Martin) at Penn State, and NSF grants (CMMI-1646660, CMMI-16171488**)**. The author (HY) also thank Harold and Inge Marcus Career Professorship for additional financial support. We gratefully acknowledge the valuable contributions of the faculty, staff, and students at Penn State's Center for Innovative Materials Processing through Direct Digital Deposition (CIMP-3D) for providing the data utilized in this research.

One of the authors (PKR) thanks the NSF for funding his work through the following grants CMMI-1719388 and CMMI-1752069 (CAREER) at University of Nebraska-Lincoln. The concept of using spectral graph theory for process monitoring in the neurophysiology domain was first proposed in CMMI-1719388, and further refined for defect detection and isolation in metal additive manufacturing applications in CMMI-1752069, wherein in the latter grant, the results from this particular publication were used as a pilot result to make the case for spectral graph theoretic in-process monitoring in LPBF. The authors finally thank the two anonymous reviewers, and associate editor – Dr. Sam Anand; their diligence, time, and insightful suggestions have gone a long way in making this work more rigorous.

References

[1] 2015, "ASTM 52900-15 Standard Terminology for Additive Manufacturing", ASTM International, West Conshohocken, PA. doi: 10.1520/ISOASTM52900-15

[2] Gibson, I., Rosen, D. W., and Stucker, B., 2010, Additive manufacturing technologies: rapid prototyping to direct digital manufacturing, Springer. doi: 10.1007/978-1-4939-2113-3

[3] O'Regan, P., Prickett, P., Setchi, R., Hankins, G., and Jones, N., 2016, "Metal Based Additive Layer Manufacturing: Variations, Correlations and Process Control," Procedia Computer Science, 96, pp. 216-224. doi: 10.1016/j.procs.2016.08.134

[4] Guo, N., and Leu, M. C., 2013, "Additive manufacturing: technology, applications and research needs," Frontiers of Mechanical Engineering, 8(3), pp. 215-243. doi: 10.1007/s11465-013-0248-8

[5] Schmidt, M., Merklein, M., Bourell, D., Dimitrov, D., Hausotte, T., Wegener, K., Overmeyer, L., Vollertsen, F., and Levy, G. N., 2017 (In-press), "Laser based additive manufacturing in industry and academia," CIRP Annals - Manufacturing Technology doi: 10.1016/j.cirp.2017.05.011

[6] Everton, S. K., Hirsch, M., Stravroulakis, P., Leach, R. K., and Clare, A. T., 2016, "Review of in-situ process monitoring and in-situ metrology for metal additive manufacturing," Materials and Design, 95, pp. 431-445. doi: 10.1016/j.matdes.2016.01.099

[7] Gorelik, M., 2017, "Additive manufacturing in the context of structural integrity," International Journal of Fatigue, 94(2), pp. 168-177. doi: 10.1016/j.ijfatigue.2016.07.005

[8] Seifi, M., Gorelik, M., Waller, J., Hrabe, N., Shamsaei, N., Daniewicz, S., and Lewandowski, J. J., 2017, "Progress Towards Metal Additive Manufacturing Standardization to Support Qualification and Certification," JOM, 69(3), pp. 439-455. doi: 10.1007/s11837-017-2265-2

[9] Grasso, M., and Colosimo, B. M., 2017, "Process defects and in situ monitoring methods in metal powder bed fusion: a review," Measurement Science and Technology, 28(4), p. 044005. doi: 10.1088/1361-6501/aa5c4f

[10] Sames, W. J., List, F., Pannala, S., Dehoff, R. R., and Babu, S. S., 2016, "The metallurgy and processing science of metal additive manufacturing," International Materials Reviews, 61(5), pp. 315-360. doi: 10.1080/09506608.2015.1116649

[11] Cheng, B., and Chou, K., 2015, "Geometric consideration of support structures in part overhang fabrications by electron beam additive manufacturing," Computer-Aided Design, 69, pp. 102-111. doi: 10.1016/j.cad.2015.06.007

[12] Aboulkhair, N. T., Everitt, N. M., Ashcroft, I., and Tuck, C., 2014, "Reducing porosity in AlSi10Mg parts processed by selective laser melting," Additive Manufacturing, 1, pp. 77-86. doi:

[13] Mahmoudi, M., Elwany, A., Yadollahi, A., Thompson, S. M., Bian, L., and Shamsaei, N., 2017, "Mechanical properties and microstructural characterization of selective laser melted 17-4 PH stainless steel," Rapid Prototyping Journal, 23(2), pp. 280-294. doi: 10.1108/RPJ-12-2015-0192

[14] Bi, G., Sun, C., and Gasser, A., 2013, "Study on influential factors for process monitoring and control in laser aided additive manufacturing," Journal of Materials Processing Technology, 213(3), pp. 463-468. doi: 10.1016/j.jmatprotec.2012.10.006

[15] Imani, F., Gaikwad, A., Montazeri, M., Yang, H., and Rao, P., 2018, "Layerwise in-Process Quality Monitoring in Laser Powder Bed Fusion," ASME Paper No. 6477 MSEC, College Station, TX.

[16] Imani, F., Yao, B., Chen, R., Rao, P., and Yang, H., 2018, "Factal pattern recognition of image profiles for manufacturing process monitoring and control," ASME Paper No. 6523 MSEC, College Station, TX.

[17] Yao, B., Imani, F., and Yang, H., 2018, "Markov Decision Process for Image-guided Additive Manufacturing," IEEE Robotics and Automation Letters. doi: 10.1109/LRA.2018.2839973

[18] Rao, S., Cunningham, R., Ozturk, T., and Rollett, A. D., 2016, "Measurement and Analysis of Porosity in Al-10Si-1Mg Components Additively Manufactured by Selective Laser Melting," Materials Performance and Characterization, 5(5), pp. 701-716. doi: 0.1520/MPC20160037

[19] Maskery, I., Aboulkhair, N. T., Corfield, M. R., Tuck, C., Clare, A. T., Leach, R. K., Wildman, R. D., Ashcroft, I. A., and Hague, R. J. M., 2016, "Quantification and characterisation of porosity in selectively laser melted Al–Si10–Mg using X-ray computed tomography," Materials Characterization, 111, pp. 193-204. doi: 10.1016/j.matchar2015.12.001

[20] Gong, H., Rafi, K., Starr, T., and Stucker, B., 2012, "Effect of defects on fatigue tests of as-built Ti-6Al-4V parts fabricated by selective laser melting," Solid freeform fabrication symposium, Austin, TX, pp. 499-506.

[21] DebRoy, T., Wei, H. L., Zuback, J. S., Mukherjee, T., Elmer, J. W., Milewski, J. O., Beese, A. M., Wilson-Heid, A., De, A., and Zhang, W., 2018, "Additive manufacturing of metallic components – Process, structure and properties," Progress in Materials Science, 92, pp. 112-224. doi: 10.1016/j.pmatsci.2017.10.001

[22] Gong, H., Rafi, K., Gu, H., Janaki Ram, G. D., Starr, T., and Stucker, B., 2015, "Influence of defects on mechanical properties of Ti–6Al–4V components produced by selective laser melting and electron beam melting," Materials & Design, 86, pp. 545-554. doi: 10.1016/j.matdes.2015.07.147

[23] Khairallah, S. A., Anderson, A. T., Rubenchik, A., and King, W. E., 2016, "Laser powder-bed fusion additive manufacturing: Physics of complex melt flow and formation mechanisms of pores, spatter, and denudation zones," Acta Materialia, 108, pp. 36-45. doi: 10.1016/j.actamat.2016.02.014

[24] Gong, H., Rafi, K., Gu, H., Starr, T., and Stucker, B., 2014, "Analysis of defect generation in Ti–6Al–4V parts made using powder bed fusion additive manufacturing processes," Additive Manufacturing, 1-4, pp. 87-98. doi: 10.1016/j.addma.2014.08.002

[25] King, W. E., Barth, H. D., Castillo, V. M., Gallegos, G. F., Gibbs, J. W., Hahn, D. E., Kamath, C., and Rubenchik, A. M., 2014, "Observation of keyhole-mode laser melting in laser powder-bed fusion additive manufacturing," Journal of Materials Processing Technology, 214(12), pp. 2915-2925. doi: 10.1016/j.jmatprotec.2014.06.005

[26] Beuth, J., Fox, J., Gockel, J., Montgomery, C., Yang, R., Qiao, H., Soylemez, E., Reeseewatt, P., Anvari, A., and Narra, S., 2013, "Process mapping for qualification across multiple direct metal additive manufacturing processes," Proceedings of the Solid Freeform Fabrication Symposium, Austin, TX.

[27] Beuth, J., and Klingbeil, N., 2001, "The role of process variables in laser-based direct metal solid freeform fabrication," JOM, 53(9), pp. 36-39. doi: 10.1007/s11837-001-0067-y

[28] Vasinonta, A., Beuth, J. L., and Griffith, M., 2007, "Process maps for predicting residual stress and melt pool size in the laser-based fabrication of thin-walled structures," Journal of Manufacturing Science and Engineering, 129(1), pp. 101-109. doi: 10.1115/1.2335852

[29] Morgan, R. H., Papworth, A. J., Sutcliffe, C., Fox, P., and O'neill, W., 2002, "High density net shape components by direct laser re-melting of single-phase powders," Journal of Materials Science, 37(15), pp. 3093-3100. doi: 10.1023/a:1016185606642

[30] Montazeri, M., Yavari, R., Rao, P., and Boulware, P., 2018, "In-process Monitoring of Material Cross-Contamination Defects in Laser Powder Bed Fusion," ASME Transactions, Journal of Manufacturing Science and Engineering, (In-Press). doi: 10.1115/1.4040543

[31] Maskery, I., Aboulkhair, N., Corfield, M., Tuck, C., Clare, A., Leach, R. K., Wildman, R. D., Ashcroft, I., and Hague, R. J., 2016, "Quantification and characterisation of porosity in selectively laser melted Al–Si10–Mg using X-ray computed tomography," Materials Characterization, 111, pp. 193-204. doi: 10.1016/j.matchar.2015.12.001

[32] Gu, H., Gong, H., Pal, D., Rafi, K., Starr, T., and Stucker, B., 2013, "Influences of energy density on porosity and microstructure of selective laser melted 17-4PH stainless steel," Proceedings of the Solid Freeform Fabrication Symposium, Austin, TX, p. 474.

[33] Rafi, H. K., Pal, D., Patil, N., Starr, T., and Stucker, B., 2014, "Microstructure and Mechanical Behavior of 17-4 Precipitation Hardenable Steel Processed by Selective Laser Melting," J. of Materi Eng and Perform, 23(12), pp. 4421-4428. doi: 10.1007/s11665-014-1226-y

[34] Rafi, H. K., Starr, T., and Stucker, B., 2013, "A comparison of the tensile, fatigue, and fracture behavior of Ti–6Al–4V and 15-5 PH stainless steel parts made by selective laser melting," Int J Adv Manuf Technol, 69(5-8), pp. 1299-1309. doi: 10.1007/s00170-013-5106-7

[35] Mani, M., Lane, B. M., Donmez, M. A., Feng, S. C., and Moylan, S. P., 2017, "A review on measurement science needs for real-time control of additive manufacturing metal powder bed fusion processes," International Journal of Production Research, 55(5), pp. 1400-1418. doi: 10.1080/00207543.2016.1223378

[36] Tapia, G., and Elwany, A., 2014, "A Review on Process Monitoring and Control in Metal-Based Additive Manufacturing," Transactions of the ASME, Journal of Manufacturing Science and Engineering, 136(6), p. 060801. doi: 10.1115/1.4028540

[37] Mani, M., Lane, B., Donmez, A., Feng, S., Moylan, S., and Fesperman, R., 2015, "NISTIR 8036: Measurement Science Needs for Real-time Control of Additive Manufacturing Powder Bed Fusion Processes," NIST, Gaithersburg, MD.

[38] Spears, T. G., and Gold, S. A., 2016, "In-process sensing in selective laser melting (SLM) additive manufacturing," Integrating Materials and Manufacturing Innovation, 5(1), p. 2. doi: 10.1016/j.phpro.2016.08.131

[39] Lane, B., Lane, B., Moylan, S., Moylan, S., Whitenton, E. P., Whitenton, E. P., Ma, L., and Ma, L., 2016, "Thermographic measurements of the commercial laser powder bed fusion process at NIST," Rapid prototyping journal, 22(5), pp. 778-787. doi: 10.1108/RPJ-11-2015-0161

[40] Reutzel, E., and Nassar, A., 2014, "A survey of sensing and control for metal-based additive manufacturing," Proceedings of the Solid Freeform Fabrication Conference, Austin, TX, pp. 309-322.

[41] Foster, B., Reutzel, E., Nassar, A., Hall, B., Brown, S., and Dickman, C., 2015, "Optical, layerwise monitoring of powder bed fusion," Proceedings of the Solid Freeform Fabrication Symposium, Austin, TX, pp. 295-307.

[42] Nassar, A., Spurgeon, T., and Reutzel, E., 2014, "Sensing defects during directed-energy additive manufacturing of metal parts using optical emissions spectroscopy," Proceedings of the Solid Freeform Fabrication Symposium, Austin, TX, pp. 278-287.

[43] Dunbar, A. J., Nassar, A. R., Reutzel, E. W., and Blecher, J. J., 2016, "A real-time communication architecture for metal powder bed fusion additive manufacturing," Proceedings of the Solid Freeform Fabrication Symposium, Austin, TX, pp. 67-80.

[44] Foster, B. K., Reutzel, E. W., Nassar, A. R., Dickman, C. J., and Hall, B. T., 2015, "A brief survey of sensing for additive manufacturing," SPIE Sensing Technology and Applications, Baltimore, MD, pp. 94890B-94890B-94810.

[45] Abdelrahman, M., Reutzel, E. W., Nassar, A. R., and Starr, T. L., 2017, "Flaw detection in powder bed fusion using optical imaging," Additive Manufacturing, 15, pp. 1-11. doi: 10.1016/j.addma.2017.02.001

[46] Boulware, P., 2016, "Final Technical Report to National Institute of Standards and Technology and National Center for Defense Manufacturing and Machining - Measurement Science Innovation Program for Additive Manufacturing: An Evaluation of In-Process Sensing Techniques Through the Use of an Open Architecture Laser Powder Bed Fusion Platform," No. NIST# 70NANB13H192 - 20140097, Edison Welding Institute (EWI), Cincinnati, OH.

[47] Berumen, S., Bechmann, F., Lindner, S., Kruth, J.-P., and Craeghs, T., 2010, "Quality control of laser- and powder bed-based Additive Manufacturing (AM) technologies," Physics Procedia, 5, pp. 617-622. doi: 10.1016/j.phpro.2010.08.089

[48] Craeghs, T., Clijsters, S., Kruth, J. P., Bechmann, F., and Ebert, M. C., 2012, "Detection of Process Failures in Layerwise Laser Melting with Optical Process Monitoring," Physics Procedia, 39, pp. 753-759. doi: 10.1016/j.phpro.2012.10.097

[49] Craeghs, T., Clijsters, S., Yasa, E., Bechmann, F., Berumen, S., and Kruth, J.-P., 2011, "Determination of geometrical factors in Layerwise Laser Melting using optical process monitoring," Optics and Lasers in Engineering, 49(12), pp. 1440-1446. doi: 10.1016/j.optlaseng.2011.06.016

[50] Jacobsmuhlen, J. z., Kleszczynski, S., Schneider, D., and Witt, G., 2013, "High resolution imaging for inspection of Laser Beam Melting systems," 2013 IEEE International Instrumentation and Measurement Technology Conference, Minneapolis, MN, pp. 707-712.

[51] Kleszczynski, S., zur Jacobsmühlen, J., Reinarz, B., Sehrt, J. T., Witt, G., and Merhof, D., 2014, "Improving process stability of laser beam melting systems," Fraunhofer Direct Digital Manufacturing Conference, Berlin, Germany.

[52] Kleszczynski, S., Zur Jacobsmühlen, J., Sehrt, J., and Witt, G., 2012, "Error detection in laser beam melting systems by high resolution imaging," Proceedings of the Twenty Third Annual International Solid Freeform Fabrication Symposium, Austin, TX, pp. 975-987.

[53] Wegner, A., and Witt, G., 2011, "Process monitoring in laser sintering using thermal imaging," SFF Symposium, Austin, Texas, USA, pp. 8-10.

[54] Calta, N. P., Wang, J., Kiss, A. M., Martin, A. A., Depond, P. J., Guss, G. M., Thampy, V., Fong, A. Y., Weker, J. N., Stone, K. H., Tassone, C. J., Kramer, M. J., Toney, M. F., Buuren, A. V., and Matthews, M. J., 2018, "An instrument for in situ time-resolved X-ray imaging and diffraction of laser powder bed fusion additive manufacturing processes," Review of Scientific Instruments, 89(5), p. 055101. doi: 10.1063/1.5017236

[55] Hu, D., and Kovacevic, R., 2003, "Sensing, modeling and control for laser-based additive manufacturing," International Journal of Machine Tools and Manufacture, 43(1), pp. 51-60. doi: 10.1016/S0890-6955(02)00163-3

[56] Barua, S., Sparks, T., and Liou, F., 2011, "Development of low-cost imaging system for laser metal deposition processes," Rapid Prototyping Journal, 17(3), pp. 203-210. doi: 10.1108/13552541111124789

[57] Krauss, H., Eschey, C., and Zaeh, M., 2012, "Thermography for monitoring the selective laser melting process," Proceedings of the Solid Freeform Fabiraction Conference, Austin, TX, pp. 999-1014.

[58] Rieder, H., Alexander, D., Spies, M., Bamberg, J., and Hess, T., 2014, "Online Monitoring of Additive Manufacturing Processes Using Ultrasound," 11th European Conference on Non-Destructive Testing (ECNDT 2014) Prague, Czech Republic.

[59] Krauss, H., Zeugner, T., and Zaeh, M. F., 2014, "Layerwise Monitoring of the Selective Laser Melting Process by Thermography," Physics Procedia, 56, pp. 64-71. doi: 10.1016/j.phpro.2014.08.097

[60] Derakhshani, M., Berfield, T., and Murphy, K. D., 2018, "Dynamic Analysis of a Bi-stable Buckled Structure for Vibration Energy Harvester," Dynamic Behavior of Materials, Volume 1, Indianapolis, IN, USA, pp. 199-208.

[61] Chiu, T.-M., Mahmoudi, M., Dai, W., Elwany, A., Liang, H., and Castaneda, H., 2018, "Corrosion assessment of Ti-6Al-4V fabricated using laser powder-bed fusion additive manufacturing," Electrochimica Acta, 279, pp. 143-151. doi: 10.1016/j.electacta.2018.04.189

[62] Melvin III, L. S., Das, S., and Beaman Jr, S., 1994, "Video Microscopy of Selective Laser Sintering," Proceedings of the Solid Freeform Fabrication Symposium, Austin, TX, pp. 34-41.

[63] Bartkowiak, K., 2010, "Direct laser deposition process within spectrographic analysis in situ," Physics Procedia, 5, pp. 623-629. doi: 10.1016/j.phpro.2010.08.090

[64] Chivel, Y., and Smurov, I., 2010, "On-line temperature monitoring in selective laser sintering/melting," Physics Procedia, 5, pp. 515-521. doi: 10.1016/j.phpro.2010.08.079

[65] Craeghs, T., Clijsters, S., Yasa, E., and Kruth, J.-P., 2011, "Online quality control of selective laser melting," Solid Freeform Fabrication Proceedings, Austin, TX, pp. 212-226.

[66] Craeghs, T., Bechmann, F., Berumen, S., and Kruth, J. P., 2010, "Feedback control of Layerwise Laser Melting using optical sensors," Physics Procedia, 5, pp. 505-514. doi: 10.1016/j.phpro.2010.08.078

[67] Heigel, J. C., and Lane, B. M., 2018, "Measurement of the Melt Pool Length During Single Scan Tracks in a Commercial Laser Powder Bed Fusion Process," Journal of Manufacturing Science and Engineering, 140(5), pp. 051012-051012-051017. doi: 10.1115/1.4037571

[68] Dunbar, A. J., and Nassar, A. R., 2018, "Assessment of optical emission analysis for in-process monitoring of powder bed fusion additive manufacturing," Virtual and Physical Prototyping, 13(1), pp. 14-19. doi: 10.1080/17452759.2017.1392683

[69] Stutzman, C. B., Nassar, A. R., and Reutzel, E. W., 2018, "Multi-sensor investigations of optical emissions and their relations to directed energy deposition processes and quality," Additive Manufacturing, 21, pp. 333-339. doi: 10.1016/j.addma.2018.03.017

[70] Montazeri, M., and Rao, P., 2018, "Heterogeneous Sensor-based Build Condition Monitoring in Laser Powder Bed Fusion Additive Manufacturing Process using a Spectral Graph Theoretic Approach," ASME Transactions, Journal of Manufacturing Science and Engineering, (In-Press). doi: 10.1115/1.4040264

[71] Hirsch, M., Patel, R., Li, W., Guan, G., Leach, R. K., Sharples, S. D., and Clare, A. T., 2016, "Assessing the capability of in-situ nondestructive analysis during layer based additive manufacture," Additive Manufacturing. doi: 10.1016/j.addma.2016.10.004

[72] Smith, R. J., Hirsch, M., Patel, R., Li, W., Clare, A. T., and Sharples, S. D., 2016, "Spatially resolved acoustic spectroscopy for selective laser melting," Journal of Materials Processing Technology, 236, pp. 93-102. doi: 10.1016/j.jmatprotec.2016.05.005

[73] Solomon, C., and Breckon, T., 2011, Fundamentals of Digital Image Processing: A practical approach with examples in Matlab, John Wiley & Sons. doi: 10.1002/9780470689776.ch9

[74] Chung, F., 1997, Spectral Graph Theory American Mathematical Society. doi: 10.1090/cbms/092

[75] Jianbo, S., and Malik, J., 2000, "Normalized cuts and image segmentation," IEEE Transactions on Pattern Analysis and Machine Intelligence, 22(8), pp. 888-905. doi: 10.1109/34.868688

[76] Rao, P. K., Beyca, O. F., Kong, Z., Bukkapatnam, S. T., Case, K. E., and Komanduri, R., 2015, "A graph-theoretic approach for quantification of surface morphology variation and its application to chemical mechanical planarization process," IIE Transactions, 47(10), pp. 1088-1111. doi: 0.1080/0740817X.2014.1001927

[77] Tootooni, M. S., Liu, C., Roberson, D., Donovan, R., Rao, P. K., Kong, Z., and Bukkapatnam, S. T. S., 2016, "Online non-contact surface finish measurement in machining using graph theory-based image analysis," Journal of Manufacturing Systems, 41, pp. 266-276. doi: 10.1016/j.jmsy.2016.09.007

[78] Mohar, B., 1991, "Eigenvalues, diameter, and mean distance in graphs," Graphs and Combinatorics, 7(1), pp. 53-64. doi: 10.1007/bf01789463

[79] Imani, F., Cheng, C., Chen, R., and Yang, H., 2018, "Nested Gaussian Process Modeling for High-dimensional Data Imputation in Healthcare Systems," IISE 2018 Conference & Expo, Orlando, FL.

[80] Jiang, X., Scott, P. J., Whitehouse, D. J., and Blunt, L., 2007, "Paradigm shifts in surface metrology. Part 2 : The current shift," Proceedings of the Royal Society A: Mathematical, Physical and Engineering Science, 463(2085), pp. 2071-2099. doi: 10.1098/rspa.2007.1873

[81] Jiang, X., Scott, P. J., Whitehouse, D. J., and Blunt, L., 2007, "Paradigm shifts in surface metrology. Part 1: Historical philosophy," Proceedings of the Royal Society A: Mathematical, Physical and Engineering Science, 463(2085), pp. 2049-2070. doi: 10.1098/rspa.2007.1874

[82] Whitehouse, D. J., 2002, Handbook of surface and nanometrology, Taylor & Francis, New York. doi: 10.1201/9781420034196

[83] Yao, B., Imani, F., Sakpal, A., Reutzel, E. W., and Yang, H., 2017, "Multifractal Analysis of Image Profiles for the Characterization and Detection of Defects in Additive Manufacturing (In-Press)," Transactions of the ASME, Journal of Manufacturing Science and Engineering. doi: 10.1115/1.4037891

[84] Kan, C., Cheng, C., and Yang, H., 2016, "Heterogeneous recurrence monitoring of dynamic transients in ultraprecision machining processes," Journal of Manufacturing Systems, 41, pp. 178-187. doi: 10.1016/j.jmsy.2016.08.007

[85] Yang, H., and Chen, Y., 2014, "Heterogeneous recurrence monitoring and control of nonlinear stochastic processes," Chaos: An Interdisciplinary Journal of Nonlinear Science, 24(1), p. 013138. doi: 10.1063/1.4869306

[86] Feder, J., 1988, Fractals, 283 pp, Plenum, New York. doi: 10.1007/978-1-4899-2124-6

[87] Meisel, L., Johnson, M., and Cote, P., 1992, "Box-counting multifractal analysis," Physical Review A, 45(10), p. 6989. doi: 10.1103/PhysRevA.45.6989

[88] Barnsley, M. F., and Demko, S., 1985, "Iterated function systems and the global construction of fractals," Proceedings of the Royal Society of London A: Mathematical, Physical and Engineering Sciences, 399(1817), pp. 243-275. doi: 10.1098/rspa.1985.0057

[89] Chhabra, A., and Jensen, R. V., 1989, "Direct determination of the f (α) singularity spectrum," Physical Review Letters, 62(12), p. 1327. doi: 10.1103/PhysRevLett.62.1327

[90] Fabio, D., Reis, A., and Riera, R., 1994, "Lacunarity calculation in the true fractal limit," Journal of Physics A: Mathematical and General, 27(6), p. 1827. doi: 10.1088/0305-4470/27/6/010

[91] Tolle, C. R., McJunkin, T. R., and Gorsich, D. J., 2008, "An efficient implementation of the gliding box lacunarity algorithm," Physica D: Nonlinear Phenomena, 237(3), pp. 306-315. doi: 10.1016/j.physd.2007.09.017

[92] Plotnick, R. E., Gardner, R. H., Hargrove, W. W., Prestegaard, K., and Perlmutter, M., 1996, "Lacunarity analysis: a general technique for the analysis of spatial patterns," Physical review E, 53(5), p. 5461. doi: 10.1103/PhysRevE.53.5461

List of Tables

Table 1	The combination of power (P), hatch spacing (H), scan velocity (V), and layer height (T) process conditions used for making the titanium alloy parts.
Table 2	Mean count of pores and its standard deviation (in brackets) of various sizes in the XCT scan image slice in various printing conditions obtained from 30 randomly sampled layers.
Table 3	Mean counts of pores and its standard deviation (in brackets) at various locations of the XCT scan image in various printing conditions.
Table 4	Accuracy of classifiers used for classification of parts using statistical, spectral graph theoretic, multifractal and lacunarity features. The numbers in parenthesis are the standard deviations from a 5-fold replication study.

Table 1: The combination of power (P), hatch spacing (H), scan velocity (V), and layer height (T) process conditions used for making the titanium alloy parts.

Process Condition (P, H, V, T = 0.060) [W, mm, mm/sec, mm]		E_A [J.mm^{-2}]	E_V [J.mm^{-3}]
P0, H0, V0	(340, 0.12, 1250,0.06)	2.27	37.8
P -25%, H0, V0	(255, 0.12, 1250,0.06)	1.70	28.3
P-50%, H0, V0	(170, 0.12, 1250,0.06)	1.13	18.8
P0, H +25%, V0	(170, 0.15, 1250,0.06)	1.81	30.1
P0, H +50%, V0	(170, 0.18, 1250,0.06)	1.51	25.1
P0, H0, V +25%	(170, 0.12, 1562,0.06)	1.81	30.1
P0, H0, V +50%	(170, 0.12, 1875,0.06)	1.51	25.1

Table 2: Mean count of pores and its standard deviation (in brackets) of various sizes in the XCT scan image slice in various printing conditions obtained from 30 randomly sampled layers.

Mean count of pores

Size	H0, V0, P0 (Nominal condition) (0.12 mm, 1250 mm/s, 340 W)	H + 25% (0.15 mm)	H + 55% (0.18 mm)	V + 25% (1562.5 mm/s)	V + 50% (1875 mm/s)	P -25% (255 W)	P - 50% (170 W)
$R_1 \sim 16$ µm	1(1)	3(2)	42(22)	3(2)	10(5)	1(1)	132(31)
$R_2 \sim 32$ µm	1(1)	1(1)	6(4)	2(2)	4(3)	1(1)	30(12)
$R_3 \sim 48$ µm	0	0	0	1(1)	1(1)	0	3(2)
$R_4 \sim 64$ µm	0	0	0	0	1(1)	0	1(1)

Table 3: Mean counts of pores and its standard deviation (in brackets) at various locations of the XCT scan image in various printing conditions.

	Mean count of pores						
Radial distance from center of image	H0, V0, P0 (Nominal condition) (0.12 mm, 1250 mm/s, 340 W)	H + 25% (0.15 mm)	H + 50% (0.18 mm)	V + 25% (1562.5 mm/s)	V + 50% (1875 mm/s)	P + 25% (255 W)	P + 50% (340 W)
L_1 = 0 – 1 mm	1(1)	1(1)	9(6)	1(2)	3(3)	1(1)	19(9)
L_2 = 1 – 2 mm	1(1)	1(1)	18(8)	2(2)	5(4)	1(1)	50(22)
L_3= 2 – 3 mm	1(1)	2(1)	19(10)	2(2)	7(5)	1(1)	56(22)
L_4= 3 – 4 mm	1(1)	1(1)	6(4)	1(1)	2(2)	1(1)	31(13)
L_5= 4 – 5 mm	1(1)	1(1)	0	1(1)	1(1)	1(1)	1(2)

Table 4: Accuracy of classifiers used for classification of parts using statistical, spectral graph theoretic, multifractal and lacunarity features. The numbers in parenthesis are the standard deviations from a 5-fold replication study.

Classifier	**Statistical features**	**(A) Spectral graph theoretic features**	**(B) Multifractal and lacunarity features**	**Combined features A+B**
Support Vector Machine	55.58% (0.58)	71.94% (0.20)	76.16% (0.30)	89.36% (0.21)
Complex Tree	54.10% (0.14)	68.02% (0.66)	68.60% (0.50)	79.98% (0.23)
Linear Discriminant Analysis	52.72% (0.34)	63.22% (0.49)	63.02% (0.08)	82.16% (0.21)
K-Nearest Neighbor	56.62% (0.50)	67.66% (0.25)	70.38% (0.27)	78.60% (0.34)
Ensemble (Bagged Trees)	51.06% (0.58)	72.50% (0.10)	72.64% (0.61)	85.86% (0.30)
Feed Forward Neural Network	49.66% (1.99)	64.62% (1.7)	66.54% (1.76)	84.40% (1.67)

List of Figures

Figure 1	The schematic diagram of the laser-based powder bed fusion (LPBF) process.
Figure 2	Schematic diagram of the location of flash-lamps and camera used to capture in-situ powder bed images [41].
Figure 3	Cropped image of the powder bed in different light schemes.
Figure 4	An overview of the methodology for analysis of offline computed tomography data, and in-situ images of powder bed fusion process.
Figure 5	Effect of process conditions on the parts as seen in XCT scan images. Pore count increases as process conditions drift from nominal conditions. Highest number of pores are seen in the part printed at P -50 % (c3).
Figure 6	An overview of the image processing methodology used to analyze the computed tomography (XCT) scan images. (a) XCT scan image of part printed with P -50 %, (b) binarization of the XCT scan image of the part, (c) complemented binary image of the XCT scan image, and (d) noise reduced XCT scan image which is used for the spatial distribution analysis.
Figure 7	An example of the procedure followed to divide XCT scan image of a part into concentric segments. (a) First segment 0 mm – 1 mm of the XCT scan image (L1), i.e., the segment that encompasses the center of the XCT scan image, (b) second segment1 mm – 2 mm of the XCT scan image (L2), (c) third segment 2 mm – 3 mm of the XCT scan image (L3), (d) fourth segment 3 mm – 4 mm of the XCT scan image (L4), and (e) last segment 4 mm – 5 mm of the XCT scan image (L5), i.e., the segment which is farthest from the center of the XCT scan image.
Figure 8	Count of pores vs. Pore size in varying process conditions. (a) In P -50 % printing condition highest number of pores are seen of size R1 (16 μm), and in P0 and P -25 % printing condition, very few pores of size R1 (16 μm) are seen. (b) In parts printed with varying hatch spacing only pores of size R1 (16 μm) and R2 (32 μm) are seen, and the highest number of pores is seen in H +50 % printing condition. (c) In comparison with other printing conditions, the lowest number of pores is seen in parts printed with varying velocity. Pores of size R1 (16 μm) are highest in number in V0, V +25 %, and V +50 % printing conditions.
Figure 9	Mean pore count vs. radius from center of image at varying process conditions. (a) Parts printed with laser power of P -50 % have highest number of pores in the third segment (L3= 2-3mm) of the XCT scan image. Parts printed with P 0 (nominal

	condition), and P -25 % have pores located in second segment (L2= 1-2 mm) of the XCT scan image. (b) In parts printed with varying hatch spacing highest number of pores are seen in the third segment (L3= 2-3 mm) of the XCT scan image in all conditions. (c) In parts printed with varying velocity highest number of pores are seen in V +50 % in the third segment (L3= 2-3 mm), and in V0 and V +25 % conditions, highest number of pores are seen in the second segment (L2= 1-2 mm) of the XCT scan images.
Figure 10	An in-situ image of part depicting the row vectors which are used for pairwise comparison.
Figure 11	Simulated trees by the multifractal iterated function system, (a) IFS tree T1, (b) IFS tree T2, (c), IFS tree T3. All three IFS trees have the same box-counting fractal dimension of 2.0449, but different multifractal spectra as shown in **Error! Reference source not found.**.
Figure 12	Multifractal spectra of IFS trees shows the self-similarity, irregularity, and non-homogeneity of fractal objects that cannot be adequately characterized using a single fractal dimension.
Figure 13	Lacunarity analysis of IFS trees describes how fractal objects fill the space that cannot be adequately captured using traditional fractal analysis.
Figure 14	The varaitions of multifractal spectra w. r. t. the Andrew's Number for 3132 layerwise images in the LPBF process.

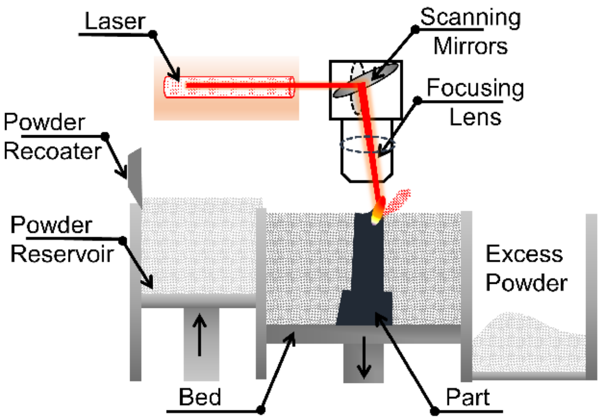

Figure 1: The schematic diagram of the laser-based powder bed fusion (LPBF) process.

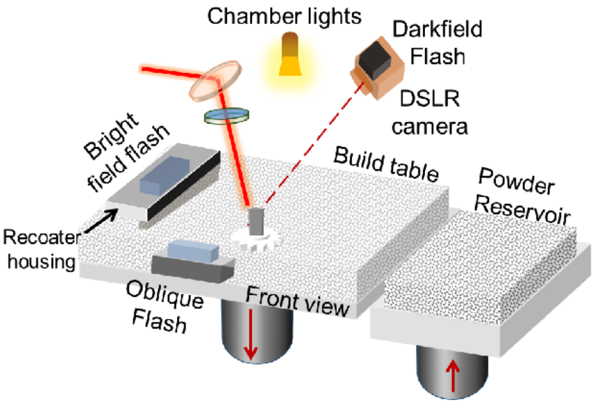

Figure 2: Schematic diagram of the location of flash-lamps and camera used to capture in-situ powder bed images [45].

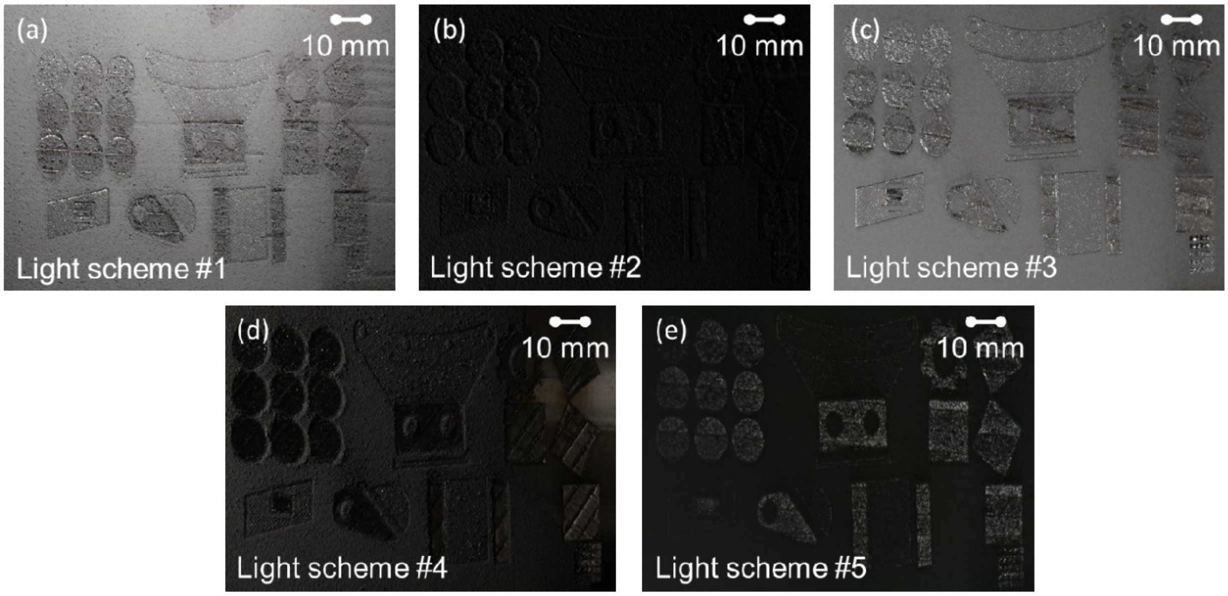

Figure 3: Cropped image of the powder bed in different light schemes.

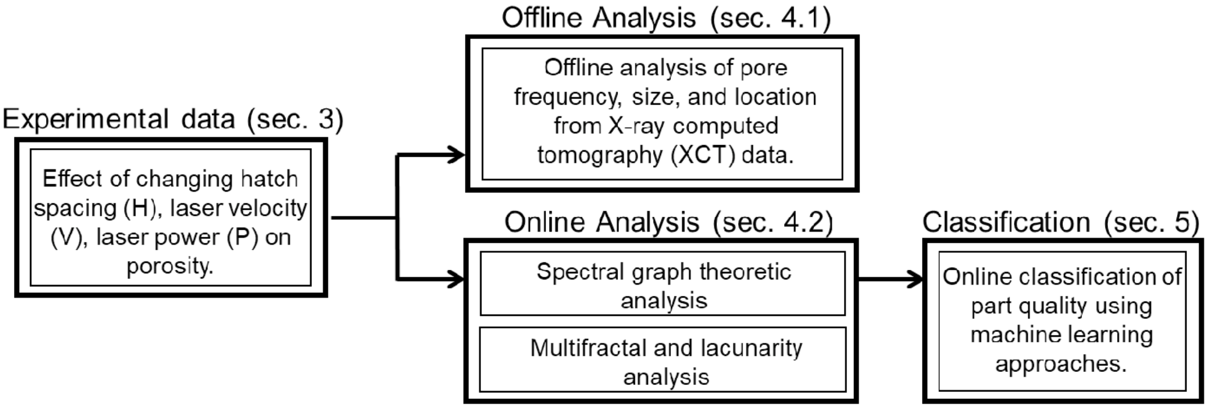

Figure 4: An overview of the methodology for analysis of offline computed tomography data, and in-situ images of powder bed fusion process.

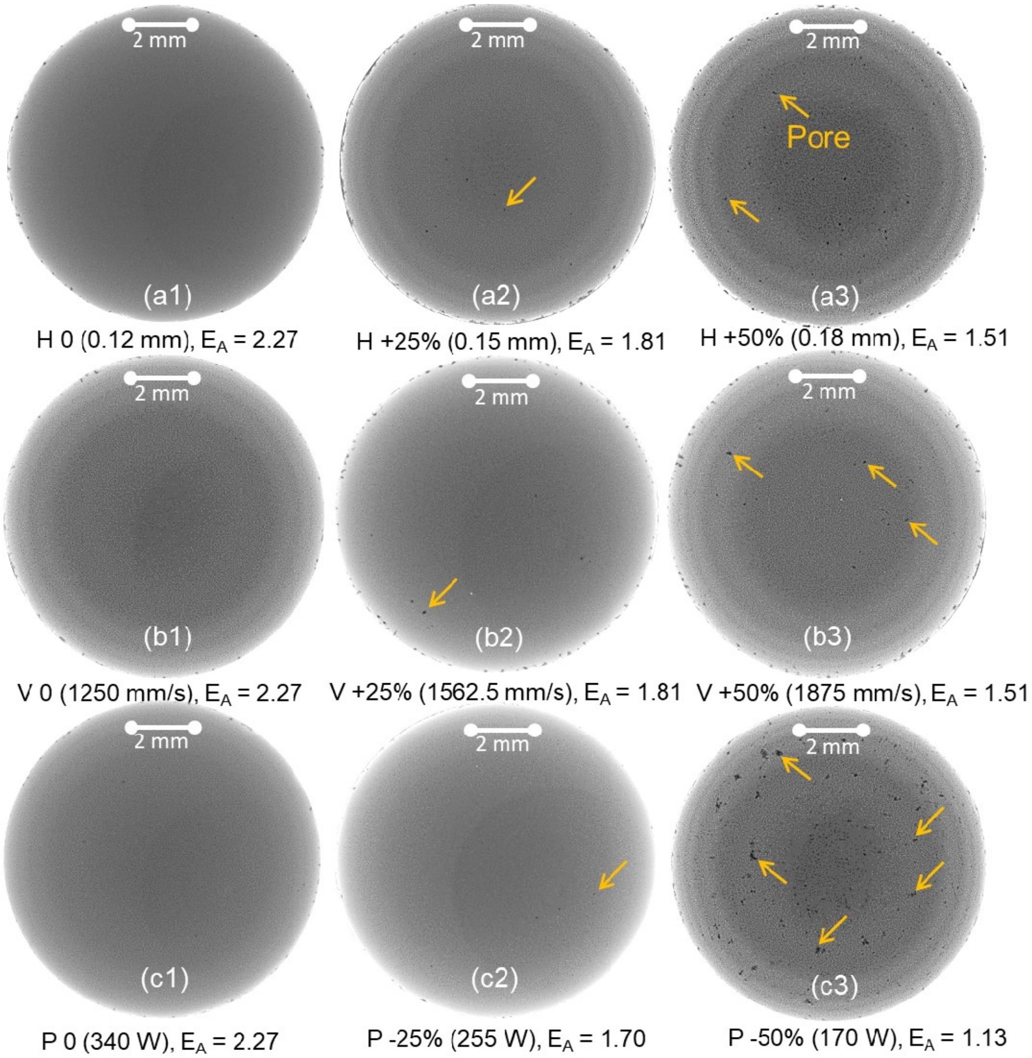

H 0 (0.12 mm), $E_A = 2.27$ H +25% (0.15 mm), $E_A = 1.81$ H +50% (0.18 mm), $E_A = 1.51$

V 0 (1250 mm/s), $E_A = 2.27$ V +25% (1562.5 mm/s), $E_A = 1.81$ V +50% (1875 mm/s), $E_A = 1.51$

P 0 (340 W), $E_A = 2.27$ P -25% (255 W), $E_A = 1.70$ P -50% (170 W), $E_A = 1.13$

Figure 5: Effect of process conditions on the parts as seen in XCT scan images. Pore count increases as process conditions drift from nominal conditions. Highest number of pores are seen in the part printed at P -50 % (c3).

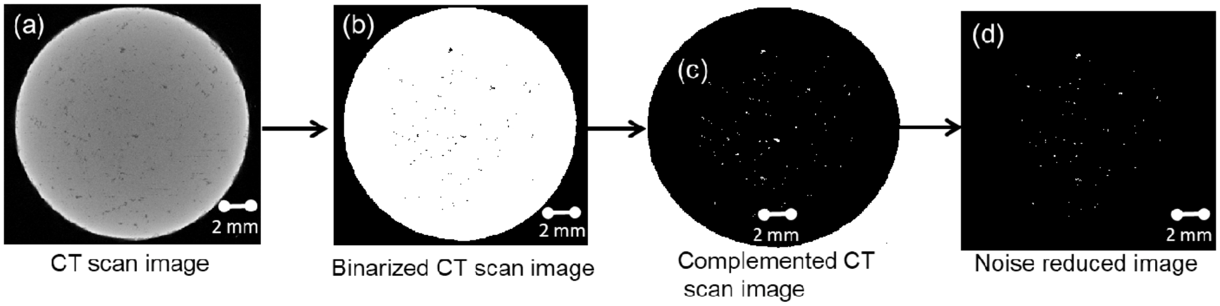

Figure 6: An overview of the image processing methodology used to analyze the computed tomography (XCT) scan images. (a) XCT scan image of part printed with P -50 %, (b) binarization of the XCT scan image of the part, (c) complemented binary image of the XCT scan image, and (d) noise reduced XCT scan image which is used for the spatial distribution analysis.

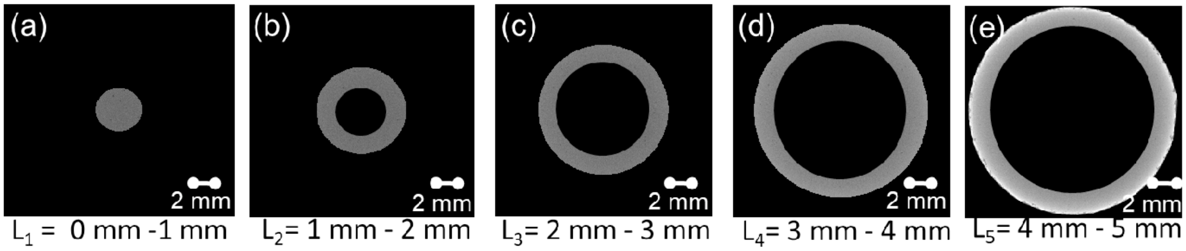

Figure 7: An example of the procedure followed to divide XCT scan image of a part into concentric segments. (a) First segment 0 mm – 1 mm of the XCT scan image (L1), i.e., the segment that encompasses the center of the XCT scan image, (b) second segment1 mm – 2 mm of the XCT scan image (L2), (c) third segment 2 mm – 3 mm of the XCT scan image (L3), (d) fourth segment 3 mm – 4 mm of the XCT scan image (L4), and (e) last segment 4 mm – 5 mm of the XCT scan image (L5), i.e., the segment which is farthest from the center of the XCT scan image.

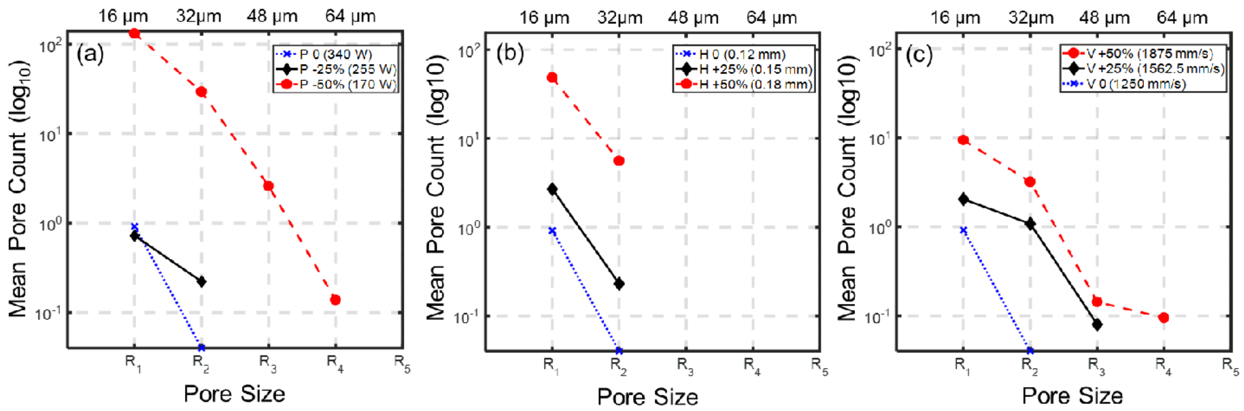

Figure 8: Count of pores vs. Pore size in varying process conditions. (a) In P -50 % printing condition highest number of pores are seen of size R1 (16 µm), and in P0 and P -25 % printing condition, very few pores of size R1 (16 µm) are seen. (b) In parts printed with varying hatch spacing only pores of size R1 (16 µm) and R2 (32 µm) are seen, and the highest number of pores is seen in H +50 % printing condition. (c) In comparison with other printing conditions, the lowest number of pores is seen in parts printed with varying velocity. Pores of size R1 (16 µm) are highest in number in V0, V +25 %, and V +50 % printing conditions.

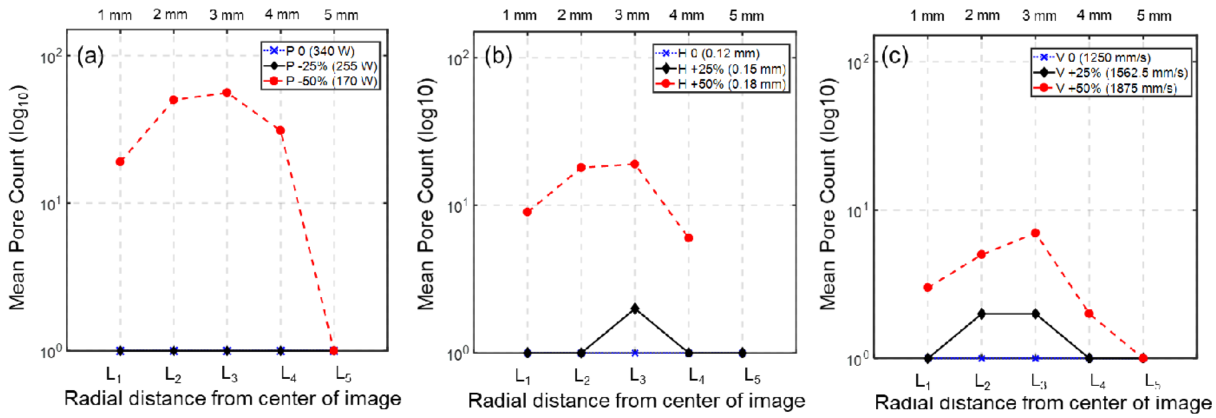

Figure 9: Mean pore count vs. radius from center of image at varying process conditions. (a) Parts printed with laser power of P -50 % have highest number of pores in the third segment (L3= 2-3mm) of the XCT scan image. Parts printed with P 0 (nominal condition), and P -25 % have pores located in second segment (L2= 1-2 mm) of the XCT scan image. (b) In parts printed with varying hatch spacing highest number of pores are seen in the third segment (L3= 2-3 mm) of the XCT scan image in all conditions. (c) In parts printed with varying velocity highest number of pores are seen in V +50 % in the third segment (L3= 2-3 mm), and in V0 and V +25 % conditions, highest number of pores are seen in the second segment (L2= 1-2 mm) of the XCT scan images.

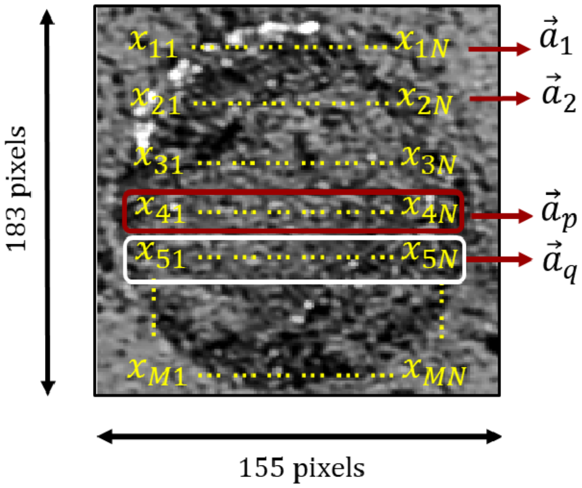

Figure 10: An in-situ image of part depicting the row vectors which are used for pairwise comparison.

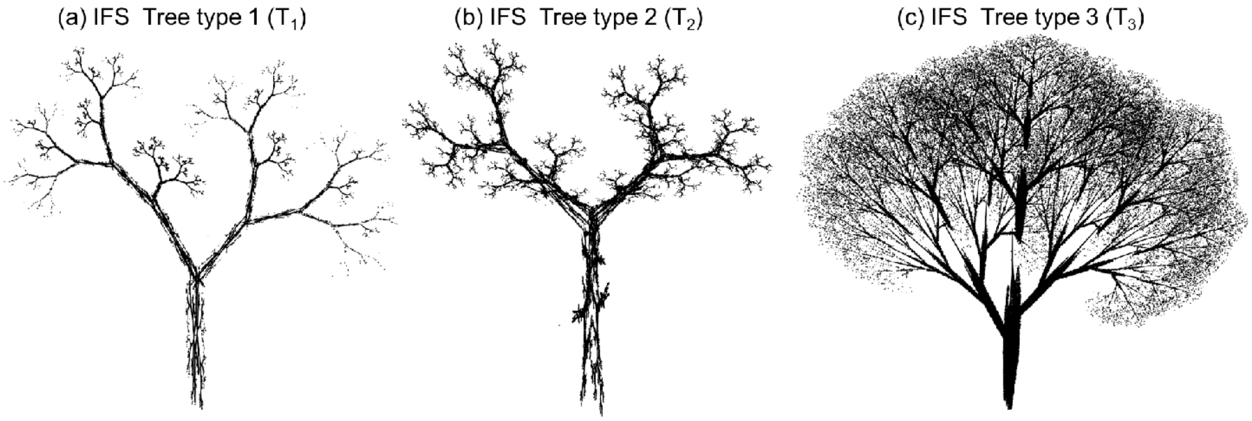

Figure 11. Simulated trees by the multifractal iterated function system, (a) IFS tree T1, (b) IFS tree T2, (c), IFS tree T3. All three IFS trees have the same box-counting fractal dimension of 2.0449, but different multifractal spectra as shown in Figure 12.

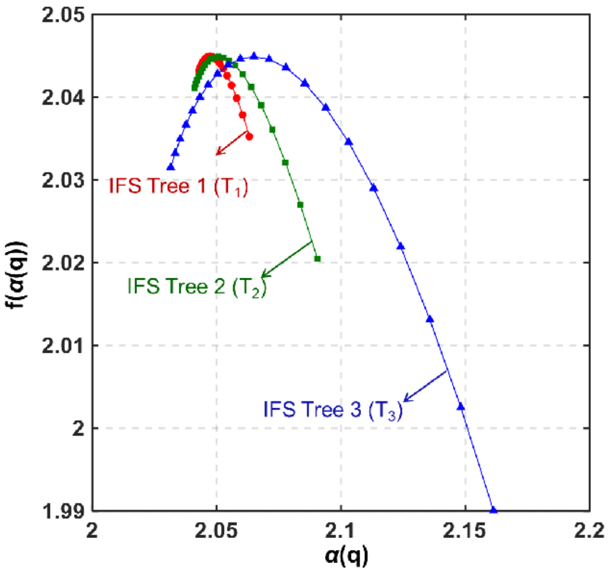

Figure 12. Multifractal spectra of IFS trees shows the self-similarity, irregularity, and non-homogeneity of fractal objects that cannot be adequately characterized using a single fractal dimension.

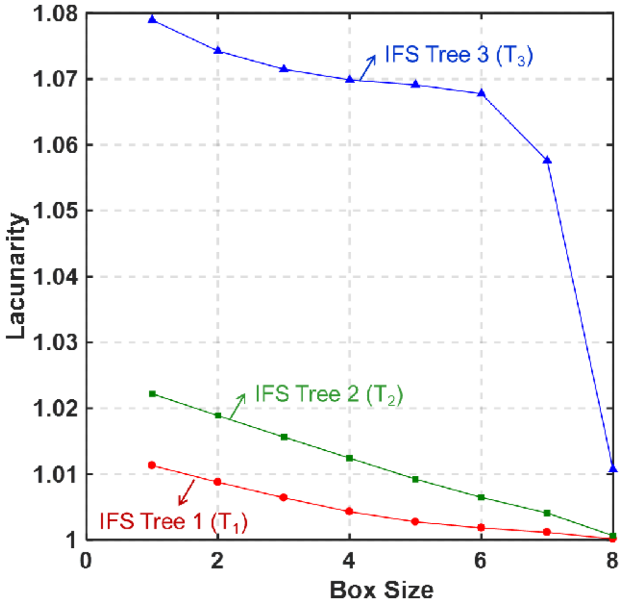

Figure 13. Lacunarity analysis of IFS trees describes how fractal objects fill the space that cannot be adequately captured using traditional fractal analysis.

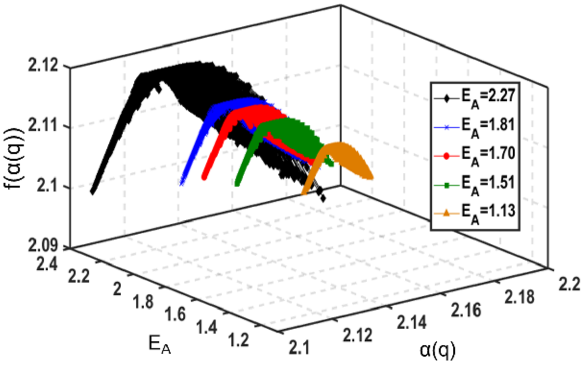

Figure 14: The variations of multifractal spectra w. r. t. the Andrew's Number for 3132 layerwise images in the LPBF process.